SCIENTIFIC REPORTS

OPEN

SUBJECT AREAS:

CHARACTERIZATION AND ANALYTICAL TECHNIQUES

MAGNETIC PROPERTIES AND MATERIALS

Received
27 March 2014

Accepted
18 June 2014

Published
11 July 2014

Correspondence and requests for materials should be addressed to D.L. (dongping.liu@dlnu.edu.cn)

* Current address: Research Center for Engineering Science, Graduate School of Engineering & Resource Science, Akita University, Gakuen Machi 1-1, Tegata, Akita, 010-8502, Japan.

# AC driven magnetic domain quantification with 5 nm resolution

Zhenghua Li[1], Xiang Li[2], Dapeng Dong[1], Dongping Liu[1], H. Saito[3]* & S. Ishio[3]

[1]Liaoning Key Lab of Optoelectronic Films & Materials, School of Physics and Materials Engineering, Dalian Nationalities University, Dalian, 116600, China, [2]School of Materials Science and Engineering, University of Shanghai for Science and Technology, Shanghai, 200093, China, [3]Venture Business Laboratory, Akita University, Gakuen Machi 1-1, Tegata, Akita, 010-8502, Japan.

**As the magnetic storage density increases in commercial products, e.g. the hard disc drives, a full understanding of dynamic magnetism in nanometer resolution underpins the development of next-generation products. Magnetic force microscopy (MFM) is well suited to exploring ferromagnetic domain structures. However, atomic resolution cannot be achieved because data acquisition involves the sensing of long-range magnetostatic forces between tip and sample. Moreover, the dynamic magnetism cannot be characterized because MFM is only sensitive to the static magnetic fields. Here, we develop a side-band magnetic force microscopy (MFM) to locally observe the alternating magnetic fields in nanometer length scales at an operating distance of 1 nm. Variations in alternating magnetic fields and their relating time-variable magnetic domain reversals have been demonstrated by the side-band MFM. The magnetic domain wall motions, relating to the periodical rotation of sample magnetization, are quantified via micromagnetics. Based on the side-band MFM, the magnetic moment can be determined locally in a volume as small as 5 nanometers. The present technique can be applied to investigate the microscopic magnetic domain structures in a variety of magnetic materials, and allows a wide range of future applications, for example, in data storage and biomedicine.**

Understanding the nature of ferromagnetism on nanometre length scales underpins the development of commercial products, such as computer hard disc drives, magnetic random access memory chips, and so on[1–6]. The development in microscopy and magnetic imaging techniques, including magneto-optical Kerr microscopy, scanning transmission X-ray microscopy, photoemission electron microscopy, Lorentz microscopy and electron holography, have facilitated the studies of magnetic domains, magnetization reversals and magnetization dynamics[7–12]. In addition, recent advances in the cavity-enhanced magneto-optic Kerr effect[13], the near-field Brillouin light scattering technique[14], ultrafast x-ray microscopy[15], and other time-resolved measurements[16,39], have further motivated the researches on magnetization dynamics of nanomagnets with superior spatiotemporal resolution. Each of these methods exhibits specific virtues, however, locally observing and quantifying the alternating magnetic field variations, and the relating time-variable magnetic domain structures with nanometer resolution, is difficult to be achieved, although these pose severe problems to the development of commercial devices[17–18].

Magnetic force microscopy (MFM) is the state-of-the-art tool used to explore the local magnetic states with superior resolution[19–23]. However, for the observations of individual device in commercial products, e.g. the magnetic write head, current MFM technique shows at least two serious drawbacks: (1) The tip-to-sample distance in MFM is far beyond the flying height of write head currently under development. The problem cannot be solved simply by reducing the lift distance, at that point MFM mixes magnetic, Van der Waals, and electrostatic forces[24–25]. (2) MFM is only sensitive to the static magnetic fields or field signals whose frequency component is close to the mechanical resonance of the cantilever ($\omega_0 = 2\pi f_0$). The magnetic fields leaking from pole tips with an operating frequency not close to $\omega_0$ cannot be detected and ultimately disappear below the detection threshold[26–27].

Here, we develop a side-band MFM method to locally observe the alternating magnetic fields, as well as the time-variable magnetic domains with 5 nm lateral resolution. This technique uses the side-band frequency modulation (FM)[28–29] of the cantilever resonance. The alternating magnetic force can periodically modulate the effective spring constant of the cantilever. The motion equation of the MFM tip can be given by

$$m\frac{d^2z(t)}{dt^2} + m\gamma\frac{dz(t)}{dt} + (k_0 + \Delta k\cos(\omega_m t))z(t) = F_0\cos(\omega_c t) \quad (1)$$

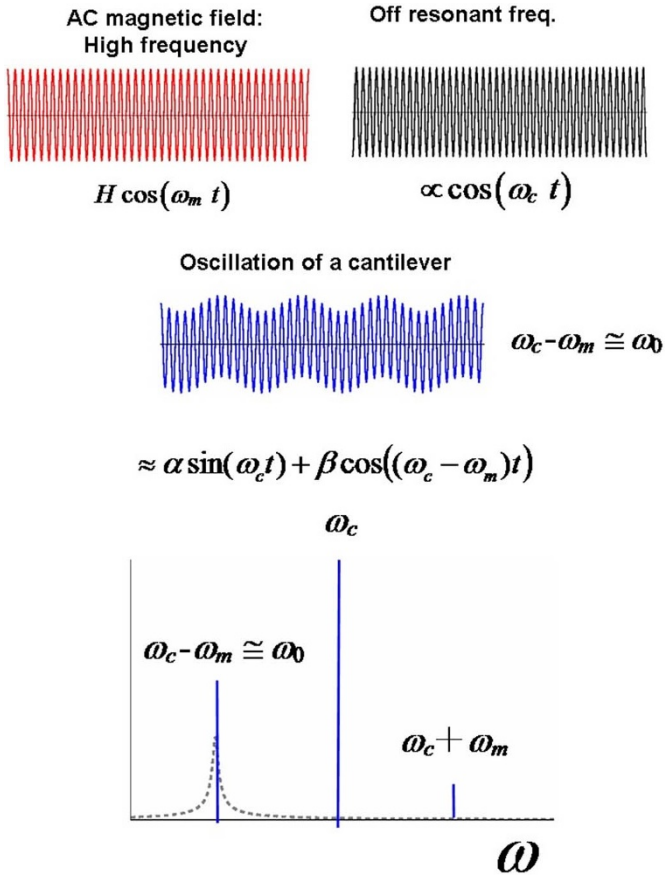


**Figure 1 | Principle of side-band frequency modulation.**

where $z$, m, $\gamma$ and $k_0$ are the displacement, effective mass, damping factor, and intrinsic spring constant of the MFM tip, respectively. Here, $\Delta k\cos(\omega_m t)$ represents the periodic change in the effective spring constant due to AC magnetic force (modulation frequency $\omega_m$), and $F_0\cos(\omega_c t)$ denotes the oscillating force driven by a piezoelectric element (driven frequency $\omega_c$). By adjusting the oscillation frequency $\omega_c$ to satisfy the condition of $\omega_c - \omega_m = \omega_0$, the cantilever displacement can be given by

$$\begin{aligned} z(t) &\cong \frac{F_0}{m\gamma\omega_0}\sin(\omega_c t) + \frac{F_0\Delta k}{2(m\gamma\omega_0)^2}\cos(\omega_0 t) = \frac{F_0}{m\gamma\omega_0}\sin(\omega_c t) \\ &+ \frac{F_0\Delta k}{2(m\gamma\omega_0)^2}\cos((\omega_c-\omega_m)t) \\ &\cong \frac{F_0}{m\gamma\omega_0}\sin\left(\omega_c t + \frac{\Delta k}{2m\gamma\omega_0}\cos(\omega_m t)\right) \\ &+ \frac{F_0\Delta k}{2(m\gamma\omega_0)^2}\sin(\omega_m t)\sin(\omega_c t) \end{aligned} \tag{2}$$

Figure 1 shows the side-band FM phenomenon in the tip oscillation formed by applying a modulation frequency of $\omega_m$. From the spectra of the tip oscillation, the intensity of the left side-band spectrum ($\omega_c - \omega_m$) increases due to the resonance of the cantilever, meanwhile, the signal of the right side-band spectrum ($\omega_c + \omega_m$) disappears owing to the mechanical filtering effect of the MFM tip. Therefore, lock-in measurement at the left side-band spectrum makes it possible to detect alternating magnetic fields with a measurable frequency up to GHz.

Figure 2 shows the schematic diagram of the side-band MFM system based on a conventional JSPM-5400 (JEOL Ltd.) scanning probe microscope. In the MFM system, the cantilever is oscillated by a piezoelectric element (oscillation frequency $f_c$), while the alternating magnetic field (driving frequency $f_m$) from the write head periodically modulates the effective spring constant of the cantilever. The frequency-modulated signals ($f = f_c \pm f_m$) are auto selected by the mechanically oscillated tip. However, only the left side-band spectra ($f_0 = f_c - f_m$) of the tip oscillation close to the resonance of the cantilever can be enhanced. The side-band signal ($f_0 = f_c - f_m$) is sensed by a photo detector with a Laser Doppler Vibrometry and fed into a lock-in amplifier as an input signal. The driving voltages of the piezo and the write head are processed by a multiplier and low pass filter, and the processed signal is used as a reference for lock-in amplifier. The vector signals of AC magnetic field gradients, such as amplitude and phase, in-phase and out-of-phase signals can be detected simultaneously by the lock-in technique. The experiment is conducted in an air atmosphere. The oscillation frequency ($f_c$) of the piezoelectric element is higher than the resonant frequency ($f_0$) of the tip. The $f_c$, $f_0$ and Q values are approximately 500 kHz, 300 kHz and 600, respectively. The sample is a trailing-edge shielded single-pole-type head (Fujitsu SPT head). The head is driven by a sinusoidal AC

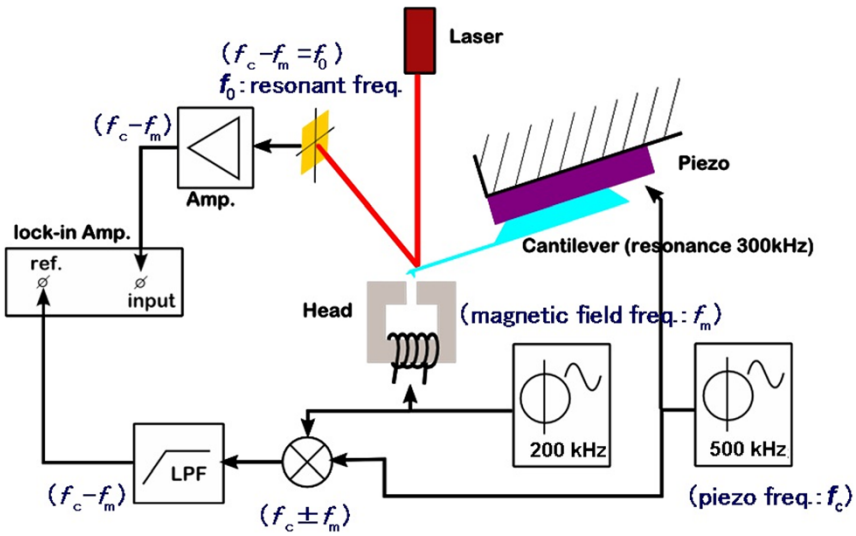


**Figure 2 | Schematic diagram of the side-band MFM system.**

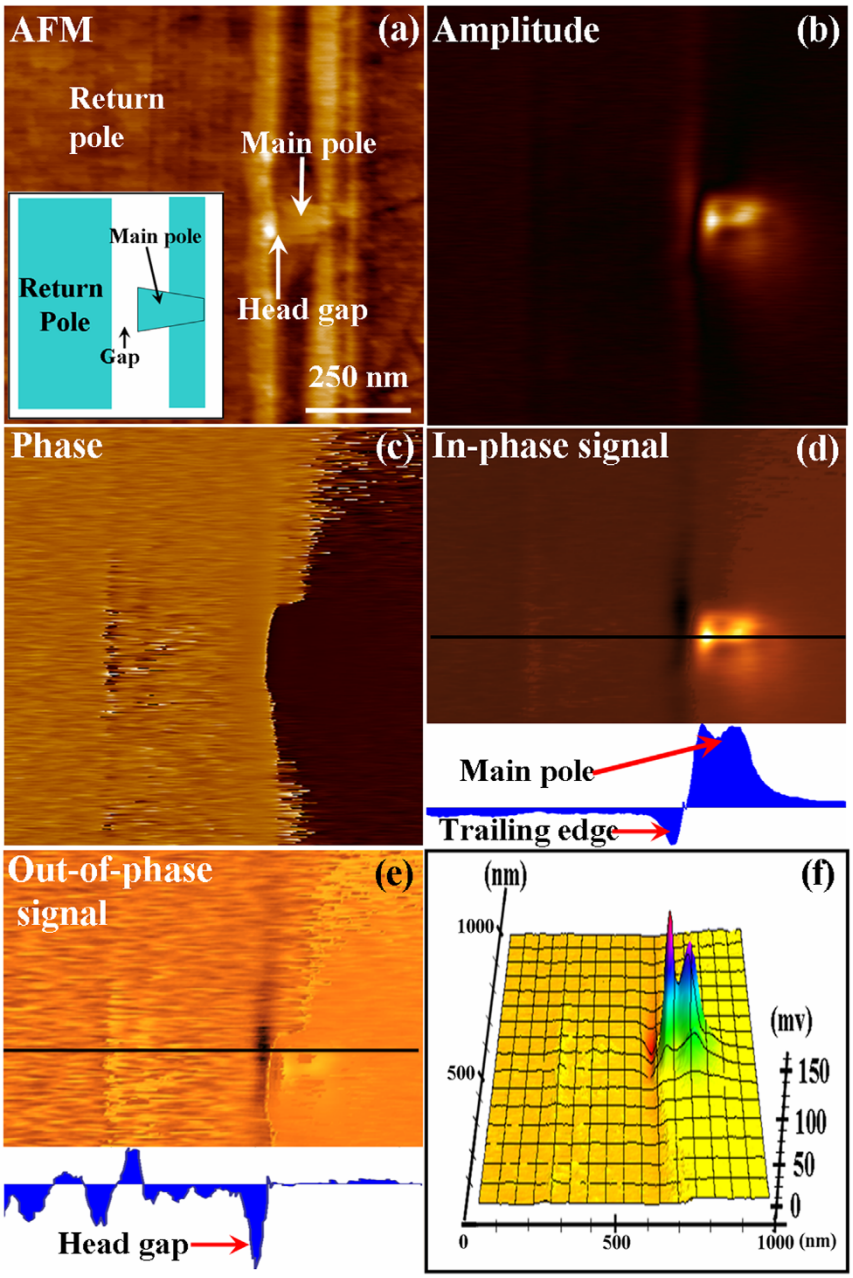


**Figure 3** | (a) Topographic image, (b) amplitude image, (c) phase image, (d) in-phase signal image, (e) out-of-phase signal image, (f) 3D image of (d), of the main pole measured by the side-band MFM technique.

current with a zero-to-peak amplitude of 20 mA and a frequency of 200 kHz. Tapping and lift mode AFM/MFM scans are carried out using a high-coercivity MFM tip (SI-MF40-Hc, Nitto Optical Co., Ltd) coated with 20 nm $L1_0$-FePt film.

Figure 3 shows the side-band MFM images of the studied write head, along with a topographic image. Figure 3(a) clearly shows a typical shielded SPT head structure with a trailing shield/return pole (The inset image shows the schematic drawing of the SPT head, and the 3-Dimensional structure of the head is shown in Supporting Information, SECTION 1). The main pole and trailing shield are embedded in the non-magnetic texture with a head gap separation. Figure 3(b) shows the corresponding amplitude image of the alternating magnetic field gradients around the main pole. It can be seen that the strong signals are formed at the pole near the edges of main pole, and the weak signal is obtained at the trailing shield near the gap. Figure 3(c) shows the corresponding MFM phase image. This image is like a two-valued image, and the phase difference between the bright and dark areas is approximately 180°. By using a high-coercivity FePt tip, we can clearly observe the positive and negative components of alternating magnetic field gradients, indicating that the magnetic forces on the MFM tip change polarity, and the magnetic field direction at the main pole is opposite to the one at the return pole/trailing shields (The side-band MFM imaging of another write head (Hitachi SPT head) is demonstrated in Supporting Information, SECTION 2).

Figures 3(d) and (e) show the measured in-phase and out-of-phase images corresponding to Figures 3(b) and (c), obtained during the same scan of the tip oscillation. The MFM in-phase image is obtained by adding an extra phase of 60° to the lock-in amplifier so that the out-of-phase signal becomes zero. In this case, the phase shift of the alternating magnetic field with respect to the driving head voltage, arising from the electronics (including the resistor-inductor circuit) and magnetics, can be compensated. The in-phase image is well characterized as the perpendicular component of alternating mag-

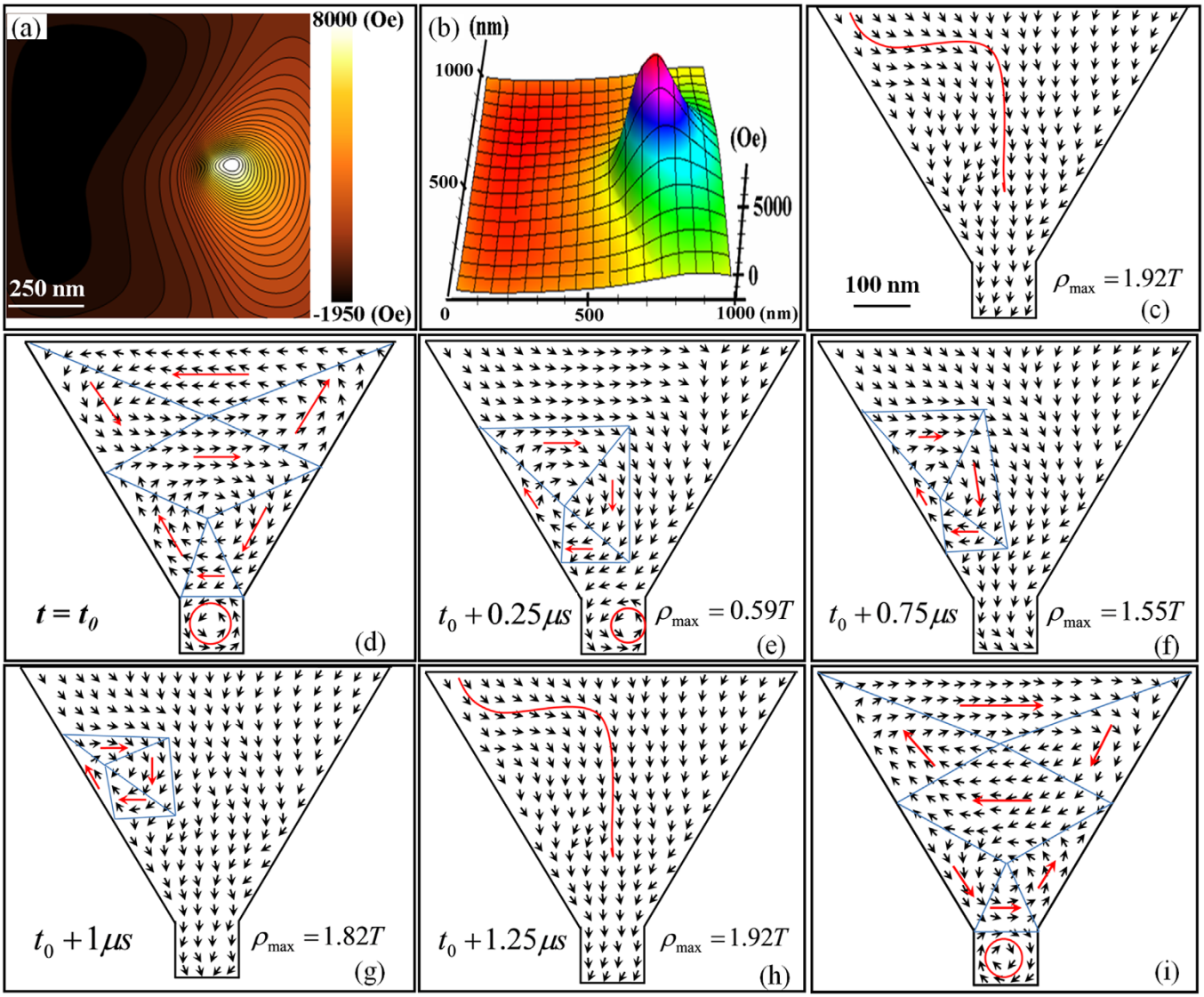


**Figure 4** | (a) The simulated magnetic field contours, (b) the simulated 3D image of (a), (c) the calculated magnetic domain structures relating to the measured in-phase image, (d)–(i) micromagnetic simulations of the time-variable magnetization process for the Fe-Co pole tip with varying magnetic driven pole densities.

netic field gradients with respect to the head surface. Meanwhile, the out-of-phase image of Figure 3(e) represents the longitudinal component of magnetic field gradients, and the enhanced contrast is only observed at the head gap. The results indicate that the magnetization at main pole rotates perpendicular to the head surface. In this case, the maximum and minimum intensities of perpendicular field gradients are obtained at the main pole/trailing shield edge. However, the maximum or minimum intensities of longitudinal field gradients are captured at the head gap, as seen in the line profiles marked in Figures 3(d) and (e). Figure 3(f) shows the corresponding 3-Dimensional (3D) image of Figure 3(d). From the 3D image, we can clearly observe the magnetic field gradients emanated from the main pole.

One way of understanding the magnetic field characteristic is to compare the measured MFM images with the simulated ones. Here, we demonstrate a deconvolution technique combined with micromagnetics, to quantify the time variable magnetic fields, as well as the detailed magnetic domain reversals in the pole tips.

The measured MFM signal is considered as the convolution of the gradient of stray magnetic field from the magnetized surface and the tip's sensitivity field, and the magnetic pole density distribution can be derived from the inverse of Fourier transformation[30–31],

$$\rho(x,y) = F^{-1}\left\{\frac{\varphi(k_x,k_y)}{G_\rho(k_x,k_y)}\right\} = \rho_{\max}\cdot\rho_i(x,y) \tag{3}$$

where $k_x$, $k_y$ are the wave vectors in Fourier space, $\varphi(k_x, k_y)$ the magnetic force gradient, $G_\rho(k_x, k_y)$ the MFM tip Green's function, $\rho_{max}$ the maximum magnetic charge density at the pole area, and $\rho_i$ the normalized magnetic charge in the $i$th cuboid mesh. The value of $\rho_{max}$ is determined by $M_n \Big/ \left[\frac{1}{N_{grids}}\sum_i \rho_i\right]$, where $N_{grids}$ is the number of grids or meshes, and $M_n$ the perpendicular magnetization calibrated by a vibrating-sample magnetometer.

By using the "magnetic monopole approximation" and assuming that the measurement is done with the constant tip-sample space (Quantification of the magnetic point monopole is described in Supporting Information, SECTION 5), the Green's function for a point magnetic monopole tip ($q_m$) with respect to a point magnetic charge can be analytically obtained in the frequency domain[32–33].

$$G_\rho(k_x,k_y,z) = -\frac{q_m}{\mu_0}\sqrt{k_x^2+k_y^2}\,e^{-\sqrt{k_x^2+k_y^2}z} \tag{4}$$

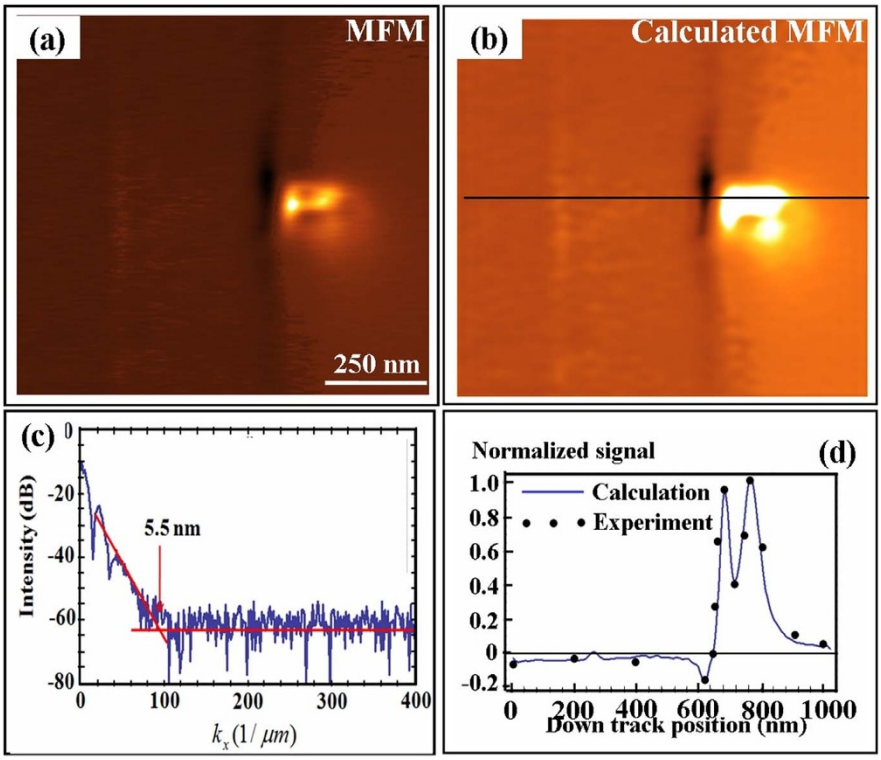


**Figure 5** | (a) The measured in-phase MFM image, (b) the calculated magnetic field gradient map, (c) Fourier spectrum of the processed MFM signal, (d) comparison between experiment and simulation.

The two-dimensional Fast Fourier Transforms (FFTs) are used to implement this algorithm numerically. A window function is used before performing the deconvolution procedure. The cut-off wave vectors of the window filter are set to $k_x = k_y = 400$ (1/μm).

After reconstruction of the magnetic charge distributions by Equation (3), we established an accurate micromagnetic model to study the magnetic domain reversals in the pole tips. In each cuboid cell, the total effective magnetic fields include the external field, the anisotropy field, the exchange field and the demagnetizing field. In the micromagnetic modeling, the magnetic pole density is treated as the input driven force for the magnetic domain evolution, and the simulations of the magnetization reversals are accomplished based on the LLG equations.

Figure 4(a) and (b) show the quantified in-phase 2D image and its corresponding 3D one exhibiting the magnetic field distributions of a Fe-Co pole tip. The magnetic field is obtained by $\vec{H}(\vec{r}) = \sum_{i=1}^{n} \frac{\rho_{\max}}{4\pi\mu_0} \frac{\rho_i(\vec{r}')(\vec{r}-\vec{r}')}{|\vec{r}-\vec{r}'|^3}$. In the calculation, the adjusted tip-to-sample distance $h = 8$ nm shows good agreement with experiment data, as shown in Figure 5(d). Compared with the operating distance $h = 1$ nm, the calculation indicates that the effective magnetic point monopole locates somewhere within the magnetic tip[34]. The value of $\rho_{max} = 1.92$ T is determined using a vibrating-sample magnetometer by applying an effective DC current to the head. This value is smaller than the saturation magnetization of the FeCo pole tip with $4\pi M_S \approx 2.4$ T, suggesting that the studied head is unsaturated when applying an AC current of 20 mA. Based on the images of Figures 4(a) and (b), we can clearly observe the alternating magnetic field ($H_z$) emanating from main pole and easily evaluate the recording performance, such as magnetic writing width, z-component of magnetic field values, $H_z$ profiles in both down-track and cross-track directions, and so on. This plays a crucial role for head design and analysis (Example of a recording process along a single track is shown in Supporting Information, SECTION 6). It is also noted that there is a big difference between Figure 4 (b) and the measured in-phase image of Figure 3(f). This can be well characterized as those of the alternating magnetic field ($H_z$) compared with its field gradients, where the magnetic field gradients are considered to be $\frac{\partial H_z}{\partial z}$. Figure 4 (c) shows the magnetic domains of the Fe-Co pole tip driven by the reconstructed magnetic pole density ($\rho_{max} = 1.92$ T). It is seen that there is no closure domains at the bottom edge of the pole tip, resulting in the leakage of a strong magnetic field from the head. It is also found that the shape of the domains is curved on the left side edge of the pole tip, indicating that the pole is not fully magnetized and the domain walls are probably pinned on the left side edge.

Figures 4(d)–(h) show the time-variable magnetization process of the Fe-Co pole tip with $\rho_{max}$ ranging from 0 to 1.92 T (The relating time-variable magnetic domain reversals are demonstrated in Supporting Information, SECTION 3). When $\rho_{max} = 0$ at the moment of $t_0$, the micromagnetic results of Figure 4(d) clearly show the closure type magnetic domains, and both the clockwise and anticlockwise rotating features are observed. In this case, no stray field can be observed around the pole tip. The first motions of the domain walls are observed when the driven magnetic pole density $\rho_{max} = 0.59$ T, as shown in Figure 4(e). The area of the domains magnetized in the driven force direction increases, and the center of the closure domains located at the bottom edge of the pole tip is shifted to the right side. These domain wall motions result in the leakage of the stray field from the pole tip. With an increase in the magnetic driven pole density (Figures 4(f)–(g)), the centers of the closure domains are shifted and disappear at the side edges of the pole tip where the domain walls are pinned. With further increasing the driven force, the domain wall moves along the side edge of the pole tip so that the stray field becomes stronger (Figures 4(h)). Figure 4(i) shows the magnetic domain image obtained from the remnant state when the driven pole density reduces to zero. It is interesting to note that the Figure 4(i) has different domain structures from those illustrated in Figure 4(d). It is presumably considered that the irreversible and hysteretic feature might be due to the

interaction between the domain wall and the side edge of the pole tip (Other possible dynamics starting from different remanent states are demonstrated in Supporting Information, SECTION 4).

Figures 5 (a) and (b) show the measured and simulated MFM images, respectively. By working out the first order derivative $\frac{\partial H_z}{\partial z}$ above head surface, we can obtain the calculated MFM image. The remarkable agreement between the simulation and experiment indicates that our method performs well. Figure 5(c) shows the spatial resolution analysis of the signal processed MFM image (Figure 5(b)). In this work, the MFM resolution is estimated from the maximum detectable frequency ($k_c$), where the intensity of MFM signal spectrum reduces to the white background level (thermodynamic noise of cantilever)[28,35–38]. The MFM resolution is estimated as half of the critical wavelength $\lambda_c = \frac{1}{2k_c}$ (The determination of spatial resolution is described in Supporting Information, SECTION 7). In Figure 5(c), the critical frequency $k_c \approx 91(1/\mu m)$, therefore, the estimated resolution is around 5 nm under the ambient condition with an operating distance of 1 nm (The accurate control of the tip-sample distance is demonstrated in Supporting Information, SECTION 8). In side-band MFM, we use a lock-in amplifier, which enables us to detect smaller AC force signal than the conventional MFM. The smaller minimal measurable force signal with its high signal amplitude and signal-to-noise ratio results in a better resolution in side-band MFM than the conventional one (The comparison between conventional MFM and side-band MFM images is demonstrated in Supporting Information, SECTION 9). Moreover, based on the side-band technique, the MFM tip may get close to the sample surface (a few nanometers) without mixing the atomic force. Therefore, we analyze the spatial resolution of MFM image with an operating distance of 1 nm. In addition, using the deconvolution technique, the processed MFM image (Figure 5(b)) shows no dependence on the tip and exhibits improved MFM signals compared to Figure 5(a).

Finally, the local observation and quantification of alternating magnetic fields, the time-variable magnetic domains, as well as the domain wall motions, have been demonstrated with a side-band MFM. Based on the side-band MFM, the magnetic moment can be determined locally in a volume as small as 5 nanometers. The present technique can be applied to investigate the microscopic magnetic domain structures in a variety of magnetic materials, such as high-density recording media (The imaging of nanoscale domain structures in a perpendicular magnetic recording media is demonstrated in Supporting Information, SECTION 8), ultrathin films, nanoparticles, patterned elements, as well as other magnetic features and nanostructures, which opens up the possibility for directly observing the alternating magnetic fields with superior spatial resolution, and sheds light on the development of next generation commercial products.

## Methods

Theory for imaging the rotation of magnetization. In side-band MFM, the SPT head is driven by an AC current, and the magnetic moment ($M^{ac}_{sample}$) of head rotates periodically near the sample surface,

$$M^{ac}_{sample}(t) = M_z(t) + M_x(t) = M^{ac}_z \cos(\omega_m t) + M^{ac}_x \sin(\omega_m t) \tag{5}$$

where $M^{ac}_z$ and $M^{ac}_x$ are the amplitudes of perpendicular and in-plane magnetization components, respectively.

When the MFM tip behaves as a monopole-type tip, the effective change in the spring constant $\Delta k$ of the cantilever is given by

$$\begin{aligned}\Delta k(t) &\cong q^{dc}_{tip}\frac{\partial H^{ac}_z(M^{ac}_{sample}(t))}{\partial z} = q^{dc}_{tip}\left(\frac{\partial H^{ac}_z(M^{ac}_z\cos(\omega_m t))}{\partial z} + \frac{\partial H^{ac}_z(M^{ac}_x\sin(\omega_m t))}{\partial z}\right)\\ &\cong q^{dc}_{tip}\left(\frac{\partial H^{ac}_z(M^{ac}_z)}{\partial z}\cos(\omega_m t) + \frac{\partial H^{ac}_z(M^{ac}_x)}{\partial z}\sin(\omega_m t)\right) = \Delta k_0\cos(\omega_m t + \phi)\end{aligned} \tag{6}$$

where $q^{dc}_{tip}$ is the DC magnetic charge at the tip end, $H^{ac}_Z$ the z-component of the alternating magnetic fields from the sample surface, $M^{ac}_{sample}$ the AC magnetic field source, and $\omega_m$ the AC frequency.

Based on the principle of side-band MFM, the motion equation of the MFM tip can be given by

$$m\frac{d^2z(t)}{dt^2} + m\gamma\frac{dz(t)}{dt} + (k_0 + \Delta k_0\cos(\omega_m t + \phi))z(t) = F_0\cos(\omega_c t) \tag{7}$$

where $z$ is the displacement of the tip in perpendicular direction, $m$ the effective mass of the tip, $\gamma$ the damping factor of the oscillation, $k_0$ the intrinsic spring constant of the cantilever and $F_0$ the force driven by a piezoelectric element with a frequency of $\omega_c$. Therefore, the cantilever displacement can be given by

$$\begin{aligned}z(t) &\cong \frac{F_0}{m\gamma\omega_0}\sin\left(\omega_c t + \frac{\Delta k_0}{2m\gamma\omega_0}\cos(\omega_m t + \phi)\right)\\ &= \frac{F_0}{m\gamma\omega_0}\sin\left(\omega_c t + \frac{q^{dc}_{tip}}{2m\gamma\omega_0}\left(\frac{\partial H^{ac}_z(M^{ac}_z)}{\partial z}\cos(\omega_m t) + \frac{\partial H^{ac}_z(M^{ac}_x)}{\partial z}\sin(\omega_m t)\right)\right)\end{aligned} \tag{8}$$

By using a lock-in detection technique, the orthogonal in-phase (X) and quadrature (Y) signals, which correspond to the cosine and sine terms of the above equation, respectively, can be detected with high sensitivity in the following equations

$$\begin{aligned}X + iY &= \frac{F_0 q^{dc}_{tip}}{2(m\gamma\omega_0)^2}\left(\frac{\partial H^{ac}_z(M^{ac}_z)}{\partial z}\cos(\omega_m t) + i\frac{\partial H^{ac}_z(M^{ac}_x)}{\partial z}\sin(\omega_m t)\right)\\ &\propto \frac{\partial H^{ac}_z(M^{ac}_z\cos(\omega_m t))}{\partial z} + i\frac{\partial H^{ac}_z(M^{ac}_x\sin(\omega_m t))}{\partial z}\end{aligned} \tag{9}$$

By adding the extra phase (or time evolution operator $e^{i\omega m\Delta t}$) to the original measured signals,

$$(X + iY)e^{i\omega_m\Delta t} \propto \frac{\partial H^{ac}_z(M^{ac}_z\cos(\omega_m(t+\Delta t))}{\partial z} + i\frac{\partial H^{ac}_z(M^{ac}_x\sin(\omega_m(t+\Delta t))}{\partial z} \tag{10}$$

Therefore, the alternating magnetic fields variations, and the relating time-variable magnetic domain reversals can be demonstrated by adding an extra phase ($\omega_m\Delta t$) to the lock-in amplifier.


1. Parkin, S. S. P., Hayashi, M. & Thomas, L. Magnetic domain-wall racetrack memory. *Science* **320**, 190–194 (2008).
2. Allwood, D. A., Xiong, G., Faulkner, C. C., Atkinson, D., Petit, D. & Cowburn, R. P. Magnetic domain-wall logic. *Science* **309**, 1688–1692 (2005).
3. Schneider, T., Serga, A. A., Leven, B., Hillebrands, B., Stamps, R. L. & Kostylev, M. P. Realization of spin-wave logic gates. *Appl. Phys. Lett.* **92**, 022505 (2008).
4. Delgado, F. & Fernández-Rossier, J. Storage of classical information in quantum spins. *Phys. Rev. Lett.* **108**, 196602 (2012).
5. Vogel, J. *et al.* Direct observation of massless domain wall dynamics in nanostripes with perpendicular magnetic anisotropy. *Phys. Rev. Lett.* **108**, 247202 (2012).
6. Liu, H., Bedau, D., Backes, D., Katine, J. A. & Kent, A. D. Precessional reversal in orthogonal spin transfer magnetic random access memory devices. *Appl. Phys. Lett.* **101**, 032403 (2012).
7. Madami, M. *et al.* Magnetization configurations in NiFe slotted rings studied by magneto-optical kerr effect and magnetic force microscopy. *IEEE Trans. Magn.* **48**, 1269–1272 (2012).
8. Cheng, C., Kaznatcheev, K. & Bailey, W. E. Stochastic limits in synchronous imaging of sub-micron magnetization dynamics using scanning transmission x-ray microscopy. *J. Appl. Phys.* **111**, 07E321-07E321-3 (2012).
9. Merazzo, K. J. *et al.* X-ray photoemission electron microscopy studies of local magnetization in Py antidot array thin films. *Phys. Rev. B.* **85**, 184427 (2012).
10. Inada, Y., Akase, Z., Shindo, D. & Taniyama, A. Lorentz microscopy of magnetic domain-wall pinning on artificially introduced holes in electrical steel sheets. *Mater Trans* **53**, 1330–1333 (2012).
11. Yamamoto, K., Hogg, C. R., Yamamuro, S., Hirayama, T. & Majetich, S. A. Dipolar ferromagnetic phase transition in $Fe_3O_4$ nanoparticle arrays observed by lorentz microscopy and electron holography. *Appl. Phys. Lett.* **98**, 072509 (2011).
12. Rhensius, J. *et al.* Imaging of domain wall inertia in permalloy half-ring nanowires by time-resolved photoemission electron microscopy. *Phys. Rev. Lett.* **104**, 067201 (2010).
13. Barman, A. *et al.* Magneto-optical observation of picosecond dynamics of single nanomagnets. *Nano Lett.* **6**, 2939–2944 (2006).
14. Jersch, J. *et al.* Mapping of localized spin-wave excitations by near-field Brillouin light scattering. *Appl. Phys. Lett.* **97**, 152502 (2010).
15. Acremann, Y. *et al.* Time-resolved imaging of spin transfer switching: beyond the macrospin concept. *Phys. Rev. Lett.* **96**, 217202 (2006).
16. Krivorotov, I. N., Emley, N. C., Sankey, J. C., Kiselev, S. I., Ralph, D. C. & Buhrman, R. A. Time-domain measurements of nanomagnet dynamics driven by spin-transfer torques. *Science* **14**, 228–231 (2005).
17. Candocia, F. M., Svedberg, E. B., Litvinov, D. & Khizroev, S. Deconvolution processing for increasing the resolution of magnetic force microscopy measurements. *Nanotechnology.* **15**, S575 (2004).
18. Piao, H. G. *et al.* Ratchet effect of domain wall motion by GHz AC magnetic field in asymmetric sawtooth-shaped ferromagnetic nanowires. *IEEE Trans. Magn.* **46**, 1844–1847 (2010).

19. Li, H., Qi, X., Wu, J., Zeng, Z., Wei, J. & Zhang, H. Investigation of $MoS_2$ and graphene nanosheets by magnetic force microscopy. *ACS Nano* **7**, 2842–2849 (2013).
20. Freire, Ó. I., Bates, J. R., Miyahara, Y., Asenjo, A. & Grütter, P. H. Tip-induced artifacts in magnetic force microscopy images. *Appl. Phys. Lett.* **102**, 022417-022417-4 (2013).
21. Takamura, Y. *et al.* Tuning magnetic domain structure in nanoscale $La_{0.7}Sr_{0.3}MnO_3$ islands. *Nano Lett.* **6**, 1287–1291 (2006).
22. Cambel, V. *et al.* High resolution switching magnetization magnetic force microscopy. *Appl. Phys. Lett.* **102**, 062405-062405-4 (2013).
23. Lin, M. N. *et al.* Enhanced ferromagnetism in grain boundary of Co-doped ZnO films: A magnetic force microscopy study. *Appl. Phys. Lett.* **98**, 212509-212509-3 (2011).
24. Lau, J. W. & Shaw, J. M. Magnetic nanostructures for advanced technologies: fabrication metrology and challenges. *J. Phys. D: Appl. Phys.* **44**, 303001 (2011).
25. Jaafar, M. *et al.* Distinguishing magnetic and electrostatic interactions by a kelvin probe force microscopy–magnetic force microscopy combination. *Beilstein J. Nanotechnol.* **2**, 552–560 (2011).
26. Martin, Y. & Wickramasinghe, H. K. Magnetic imaging by "force microscopy" with 1000 Å resolution. *Appl. Phys. Lett.* **50**, 1455–1457 (1987).
27. Koblischka, M. R., Wei, J. D. & Hartmann, U. Optimization of the HF-MFM technique. *J. Phys. Conf. Ser.* **61**, 591 (2007).
28. Albrecht, T. R., Grutter, P., Horne, D. & Rugar, D. Frequency modulation detection using high-*Q* cantilevers for enhanced force microscope sensitivity. *J. Appl. Phys.* **69**, 668 (1991).
29. Li, Z. H., Hatakeyama, K., Egawa, G., Yoshimura, S. & Saito, H. Stroboscopic imaging of an alternating magnetic field from a perpendicular magnetic recording head by frequency-modulated magnetic force microscopy. *Appl. Phys. Lett.* **100**, 222405 (2012).
30. Chang, T. *et al.* Deconvolution of magnetic force images by Fourier analysis. *IEEE Trans. Magn.* **28**, 3138–3140 (1992).
31. Madabhushi, R., Gomez, R. D., Burke, E. R. & Mayergoyz, I. D. Magnetic biasing and MFM image reconstruction. *IEEE Trans. Magn.* **32**, 4147–4149 (1996).
32. Saito, H., Chen, J. & Ishio, S. Description of magnetic force microscopy by three-dimensional tip Green's function for sample magnetic charges. *J. Magn. Magn. Mater.* **191**, 153 (1999).
33. Saito, H., Chen, J. & Ishio, S. Principle of magnetic field analysis by MFM signal transformation and its application to magnetic recording media. *IEEE Trans. Magn.* **35**, 3992 (1999).
34. Hartmann, U. The point dipole approximation in magnetic force microscopy. *Phys. Lett. A.* **137**, 475 (1989).
35. Hug, H. J. *et al.* Quantitative magnetic force microscopy on perpendicularly magnetized samples. *J. Appl. Phys.* **83**, 5609–5620 (1998).
36. Hopster, H. & Oepen, H. P. Magnetic Microscopy of Nanostructures. *Springer* 265 (2005).
37. Gao, L. *et al.* Focused ion beam milled CoPt magnetic force microscopy tips for high resolution domain images. *IEEE Trans. Magn.* **40**, 2194–2196 (2004).
38. Saito, H., Van Den Bos, A. G., Abelmann, L. & Lodder, J. C. High-resolution MFM: simulation of tip sharpening. *IEEE Trans. Magn.* **39**, 3447–3449 (2003).
39. Rana, B. *et al.* Detection of picosecond magnetization dynamics of 50 nm magnetic dots down to the single dot regime. *ACS Nano.* **5**, 9559–9565 (2011).


## Acknowledgments

This research was supported by the National Natural Science Foundation of China (Grant Nos. 61103148,51202146), the 2013 Program for Liaoning Excellent Talents in University (Grant No. LJQ2013129), the 46th Scientific Research Foundation for the Returned Overseas Chinese Scholars, the National Magnetic Confinement Fusion Program (Key Project No. 2011GB108011). The authors would like to thank Professor S. Yoshimura from Akita University for providing the MFM tips. The work was also supported by JST-SENTAN of japan.

## Author contributions

Z.L. and D.L. designed the study. Z.L. and X.L. carried out the side-band MFM measurement and prepared figures 1–5. Z.L., D.D., H.S. and S.I. analyzed the results and revised the paper. Z.L. and D.L. wrote the paper. All authors reviewed the manuscript.

## Additional information

**Supplementary information** accompanies this paper at http://www.nature.com/scientificreports

**Competing financial interests**: The authors declare no competing financial interests.

**How to cite this article:** Li, Z. *et al.* AC driven magnetic domain quantification with 5 nm resolution. *Sci. Rep.* **4**, 5594; DOI:10.1038/srep05594 (2014).

This work is licensed under a Creative Commons Attribution-NonCommercial-ShareAlike 4.0 International License. The images or other third party material in this article are included in the article's Creative Commons license, unless indicated otherwise in the credit line; if the material is not included under the Creative Commons license, users will need to obtain permission from the license holder in order to reproduce the material. To view a copy of this license, visit http://creativecommons.org/licenses/by-nc-sa/4.0/